

Investigating Support Effects on Potassium-Promoted Mo₂C Catalysts for the Reverse Water Gas Shift Reaction

CAMERON F. HOLDER

JAMES R. MORSE

HEATHER D. WILLAUER

*Materials and Sensors Branch
Materials Science and Technology Division*

PATRICK M. BARBOUN

*NRC Postdoctoral Research Associate
Washington, DC*

ANDREW R. SHABAEV

*Materials Physics and Chemistry Section
Materials Science and Technology Division*

JEFFREY W. BALDWIN

*Functional Materials and Energy Section
Acoustic Division*

June 25, 2023

REPORT DOCUMENTATION PAGE

Form Approved
OMB No. 0704-0188

Public reporting burden for this collection of information is estimated to average 1 hour per response, including the time for reviewing instructions, searching existing data sources, gathering and maintaining the data needed, and completing and reviewing this collection of information. Send comments regarding this burden estimate or any other aspect of this collection of information, including suggestions for reducing this burden to Department of Defense, Washington Headquarters Services, Directorate for Information Operations and Reports (0704-0188), 1215 Jefferson Davis Highway, Suite 1204, Arlington, VA 22202-4302. Respondents should be aware that notwithstanding any other provision of law, no person shall be subject to any penalty for failing to comply with a collection of information if it does not display a currently valid OMB control number. **PLEASE DO NOT RETURN YOUR FORM TO THE ABOVE ADDRESS.**

1. REPORT DATE (DD-MM-YYYY) 23-06-2023			2. REPORT TYPE NRL Memorandum Report		3. DATES COVERED (From - To) 22/11/2021 – 22/11/2022	
4. TITLE AND SUBTITLE Investigating Support Effects on Potassium-Promoted Mo ₂ C Catalysts for the Reverse Water Gas Shift Reaction					5a. CONTRACT NUMBER	
					5b. GRANT NUMBER	
					5c. PROGRAM ELEMENT NUMBER NISE	
6. AUTHOR(S) Cameron F. Holder, James R. Morse, Patrick M. Barboun*, Andrew R. Shabaev, Jeffrey W. Baldwin, and Heather D. Willauer					5d. PROJECT NUMBER	
					5e. TASK NUMBER	
					5f. WORK UNIT NUMBER N20Z	
7. PERFORMING ORGANIZATION NAME(S) AND ADDRESS(ES) Naval Research Laboratory 4555 Overlook Avenue, SW Washington, DC 20375-5320					8. PERFORMING ORGANIZATION REPORT NUMBER NRL/6360/MR--2023/4	
9. SPONSORING / MONITORING AGENCY NAME(S) AND ADDRESS(ES) Naval Research Laboratory 4555 Overlook Avenue, SW Washington, DC 20375-5320					10. SPONSOR / MONITOR'S ACRONYM(S) NRL-NISE	
11. SPONSOR / MONITOR'S REPORT NUMBER(S)						
12. DISTRIBUTION / AVAILABILITY STATEMENT DISTRIBUTION STATEMENT A: Approved for public release; distribution is unlimited.						
13. SUPPLEMENTARY NOTES *NRC Postdoctoral Research Associate Karles Fellowship						
14. ABSTRACT The reverse water gas shift reaction (RWGS) is an important first step in the thermochemical transformation of CO ₂ to fuels. Recent research efforts have investigated transition metal carbides due to their high activity and terrestrial abundance. In order to improve particle dispersion and mechanical stability, the catalysts are often deposited onto high surface area metal oxide supports. Understanding the influence the oxide support has on the observed catalytic activity is imperative for increased efficiency. Herein, we investigate the effect of the oxide support's (γ -Al ₂ O ₃ , SiO ₂ , ZrO ₂ , CeO ₂ , and MgO) reducibility and acidity on potassium promoted molybdenum carbide catalysts for the RWGS. Additionally, DFT computation was used to evaluate CO and CO ₂ adsorption energies at a model interface of Mo ₂ C/MgO. It is demonstrated that non-reducible and acidic supports are the most active for the production of CO with K-Mo ₂ C/Al ₂ O ₃ showing the highest CO site time yield of 55.6 min ⁻¹ .						
15. SUBJECT TERMS Reverse water gas shift Molybdenum carbide Supported catalysts Heterogeneous catalysis						
16. SECURITY CLASSIFICATION OF:				17. LIMITATION OF ABSTRACT U	18. NUMBER OF PAGES 25	19a. NAME OF RESPONSIBLE PERSON Cameron Holder
a. REPORT U	b. ABSTRACT U	c. THIS PAGE U	19b. TELEPHONE NUMBER (include area code) (239) 777-1504			

This page intentionally left blank.

Investigating Support Effects on Potassium-Promoted Mo₂C Catalysts for the Reverse Water Gas Shift Reaction

Contents

Executive Summary	E-1
1.0 Background	1
2.0 Objective	2
3.0 Experimental	3
3.1 Materials	3
3.2 Catalyst Preparation	3
3.3 Catalyst Testing	3
3.4 Materials Characterization	4
3.5 Computational Modelling	5
4.0 Results and Discussion	6
4.1 Synthesis and Characterization	6
4.2 Catalytic Results	9
4.3 DFT Modelling	13
5.0 Conclusions	15
6.0 References	15

This page intentionally left blank.

Executive Summary:

The utilization of environmental CO₂ is important to not only mitigate the negative impacts from greenhouse gas emissions but can also provide the Navy with logistical and strategical advantages by enabling methods to produce value-added products, such as fuel, when and where it is needed. The direct ocean capture of CO₂ and its subsequent utilization in thermochemical or synthetic pathways thus enables a greater “Freedom of Action” for the warfighter. The reverse water gas shift reaction (RWGS) transforms CO₂ into CO, a more chemically reactive intermediate, which can be further processed into longer chain hydrocarbons. Therefore, the RWGS is often regarded as an important first step towards a commercialized process that would leverage environmental CO₂ sources such as seawater. To this end, prior reports have investigated supported transition metal carbides, particularly Mo₂C and WC, for their noble metal like activity and high selectivity when promoted by alkali metals for the low temperature (<300 °C) RWGS. Here, we present the synthesis, characterization, and catalytic evaluation of potassium promoted Mo₂C supported on various transition metal oxides to examine any correlation between the support’s acidity and reducibility on the observed catalytic activity. Of the catalysts tested, the acidic and irreducible K-Mo₂C/Al₂O₃ catalyst demonstrated the highest site time yield of 55.1 min⁻¹. Furthermore, reducible or basic supports show severely diminished catalytic activity.

This page intentionally left blank.

1.0 Background:

The limited supply of non-renewable energy sources, coupled with the current lack of renewable energy infrastructure, have prompted research efforts to establish alternative methods to produce hydrocarbon fuels and chemicals.¹⁻⁶ A potential avenue towards achieving renewable fuel and chemical production is through the recycling and conversion of CO₂ via electrochemical and/or thermal processes.⁶⁻⁸ Furthermore, efficient CO₂ capture and utilization is becoming increasingly prioritized by the U.S. DoD as it moves towards developing methods to generate fuel “near or at the point of use” which will both assist in the development of climate-resilient supply chains and offer significant logistical, operational, and cost advantages.^{9,10} To address this, the Naval Research Laboratory has recently developed a method that electrolytically extracts CO₂ from seawater while simultaneously produces H₂. These gases can be subsequently used as feedstocks for the thermocatalytic production of fuel.¹¹⁻¹⁷

An important reaction in the overall utilization of CO₂ is its reduction to CO via the RWGS reaction (Equation 1), as the product CO can be further reduced to longer chain hydrocarbons through the Fischer-Tropsch synthesis. The RWGS reaction, being endothermic, is equilibrium-limited such that higher temperatures drive the reaction towards higher conversions. For instance, the equilibrium conversion of CO₂ to CO at 300 °C for a 3:1 H₂:CO₂ blend is ~23 % while an increase in temperature to 600 °C results in CO₂ conversions of ~60 %.¹⁸ While large CO₂ conversions can thus be achieved with elevated temperatures, this also requires greater energy inputs which often result in accelerated deactivation of the catalyst and constrains the design and operation of the reactor.^{16,19-22} While lower operating temperatures can help mitigate these negative consequences, decreased conversion rates due to equilibrium limitations, as well as competing reactions such as CO₂ methanation (Equation 2), reduce the reaction efficiency.^{23,24} This emphasizes the need for RWGS catalysts that provide both high activity and high CO selectivity over a range of operating temperatures in order to most efficiently utilize the CO₂ and H₂ precursors.



Noble metals and noble metal containing alloys such as Pt, Pd, Pt-Co, and Pd-In among many others have been shown to be active catalysts for the RWGS reaction though the use of these materials on larger scales is prohibited by cost.²⁵⁻²⁸ Research efforts have thus focused on finding alternatives to noble metal catalysts. Recently, transition metal carbides, such as molybdenum and tungsten, have attracted significant attention, as they exhibit activity that mimics the activity of noble metals for a variety of catalytic reactions.²⁹⁻³¹ For example, Mo₂C has been reported as a catalyst for many reactions including CO₂ hydrogenation,^{32,33} methane reforming and aromatization,³⁴⁻³⁷ the hydrogen evolution reaction,^{38,39} and the RWGS reaction.^{16,30} In particular, Porosoff et al. reported that potassium promoted Mo₂C supported on γ-alumina was an excellent catalyst for the RWGS reaction, demonstrating a CO₂ conversion of 18.1% at 300 °C and 19.4 bar with

a CO selectivity of 95.9%.¹⁶ Additionally, Morse et al. demonstrated that alkali promoted WC supported on γ -Al₂O₃ exhibited a CO₂ conversion of 20.3% while still maintaining a high CO selectivity of 98.1% at 350 °C.¹⁷

High surface area oxide supports, such as silica and alumina, are commonly used in thermo-catalytic processes to generate well dispersed catalysts with large active surface areas, and can help to improve the thermal and mechanical stability of the catalyst. Additionally, the chemical nature of the support, and its interaction with the catalytic material, can also influence both the catalytic mechanism and the catalyst performance.^{40–43} For instance, Pt and Cu that are deposited onto reducible oxides, such as CeO₂ and TiO₂, often exhibit improved turnovers for the RWGS when compared to the same catalyst deposited onto non-reducible oxides such as Al₂O₃. This improvement is often attributed to the production of oxygen vacancies that emerge from the reduction of metal cations in the support due to the H₂ reactant. The adsorption of CO₂ to the oxygen vacancy reoxidizes the support and simultaneously generates CO, closing the catalytic cycle.^{44–48} In addition to reducibility, acidic or basic sites on the support can also significantly affect the catalytic conversion and selectivity.^{49–53} Juneau et al. recently demonstrated that Mo₂C supported on aluminosilicate zeolites with various Si/Al ratios were highly dependent on the Lewis acid site density, with larger densities being correlated to larger CO yields.⁵³ Furthermore, Sakurai et al. showed that the product selectivity for CO₂ reduction on Au catalysts could be controlled to produce either methanol or CO depending on whether a basic or acidic support was used.⁵⁴ While the influence of catalyst support has been studied for pure metals and metallic alloys, support interactions with carbide catalysts, specifically for the RWGS reaction, has received considerably less attention.

Herein, we report the activity of potassium promoted Mo₂C supported on various metal oxides to investigate the influence of support reducibility and acidity on the CO site time yields and product selectivity for the RWGS reaction. We show that K-Mo₂C is significantly more active when supported on non-reducible supports such as γ -Al₂O₃ when compared to reducible supports like CeO₂. The observed activity also correlated well with the support acidity with more acidic supports exhibiting higher CO site time yields.

2.0 Objective:

The objective of this work was to probe how the acidity and reducibility of transition metal oxide supports affected the activity of potassium promoted Mo₂C catalysts for the low temperature reverse water gas shift reaction. The results from this study will help to direct future research efforts in regards to the efficient utilization of environmental CO₂ by identifying active and selective catalyst-support combinations. Additionally, important support characteristics were identified which will help to further develop more efficient RWGS catalysts in future studies.

3.0 Experimental:

3.1 Materials:

All chemicals were used as purchased without further purification. Ammonium molybdate tetrahydrate (99.98%), potassium carbonate (99.0%), zirconium(IV) oxide (ZrO₂, nanopowder), magnesium oxide (MgO, 99.0%), cerium(IV) oxide (CeO₂, >99.95%), titanium dioxide (TiO₂, 325 mesh), and silicon(IV) dioxide (SiO₂, 200-400 mesh) were purchased from Sigma-Aldrich. Aluminum oxide (γ -Al₂O₃, 97%) was purchased from Strem Chemicals. The catalytic reactors utilized a packed bed configuration and were made from 1/4" 316L stainless steel tubing purchased from Swagelok. Gases including hydrogen (99.999%), nitrogen (99.9995%), and carbon dioxide (99.5%), were purchased through Earlebeck Gases and Technology while UHP methane (99.97%) was purchased through Matheson.

3.2 Catalyst Preparation:

Catalysts were prepared using an evaporation deposition method. For all catalyst materials, the weight percentages of K and Mo were 2% and 19%, respectively. To accomplish this, 4.70 g of ammonium molybdate tetrahydrate and 0.48 g of potassium carbonate were dissolved in 200 mL of DI water under constant stirring. Once dissolved, 10 g of the support powder was added to the stirring solution and left to evaporate overnight at 90 °C. The dry powder was homogenized with a mortar and pestle before being loaded into alumina crucibles and calcined in air to form molybdenum oxides at temperatures ranging from 350-600 °C depending on the support.

The calcined powders were ground with a mortar and pestle before approximately 1.0 g of the powder was transferred into an aluminum crucible boat. The impregnated and calcined powder was then carburized under flowing CH₄ and H₂ at temperatures ranging from 650 to 750 °C depending on the support. The flowrates of CH₄ and H₂ were 60 and 240 mL/min, respectively. Gas chromatography was used to monitor reaction progress via the evolution of CO gas. Upon the loss of CO signal, the furnace was cooled to 600 °C, the CH₄ flowrate was shut off, and the supported catalysts were treated under flowing H₂ for 1 hour to remove deposited carbon. After an hour under flowing H₂, the furnace was cooled to room temperature and the surface was passivated for a minimum of one hour with a stream of 1% O₂/N₂ flowing at 10 mL/min.

3.3 Catalyst Testing:

Prior to catalytic testing, the carburized powders were pressed into pellets and then sieved to obtain a powder with particle sizes ranging between 255 and 315 μ m. A 1/4" stainless steel reactor was loaded with 0.335 g of the size-selected carburized catalyst with glass wool acting as plugs at both ends. The catalyst bed was reduced for 90 minutes at 300 °C and 6.9 bar of H₂ which was set at a flowrate of 50 mL/min. The pressure was then increased to 19.3 bar with a mixture of N₂, H₂, and CO₂ where the ratio of H₂:CO₂ was 3:1 and N₂, used as an internal standard, comprised 16.5% of the gaseous mixture.

Gaseous flowrates were controlled using programmable Brooks Mass Flow controllers and the total flowrate was varied depending on the desired WHSV. The reactor effluent was passed through a cold trap set at 5 °C in order to remove any water prior to GC characterization. The effluent reactor stream was monitored by an Agilent 7890A online gas chromatograph and all data reported herein were collected after steady state conditions had been reached. Carbon balances between 95% and 100% were observed for all reported reactor data.

3.4 Materials Characterization:

Scanning electron microscopy (SEM) was performed using a Carl Zeiss Supra 55 microscope equipped with Schottky thermal field emission. Images were obtained at an accelerating voltage of 3 keV with an average working distance of 7 mm and a 30 μm aperture. X-ray energy dispersive spectroscopy (EDS) maps were obtained using a Princeton Gamma Tech EDS detector at accelerating voltages of 10 keV and working distance of 15 mm.

Powder X-ray diffraction (XRD) patterns were obtained using a Rigaku Smartlab X-ray diffractometer using Cu K α radiation ($\lambda = 1.5406 \text{ nm}$) over a 2θ range of 10–80°. Experimental patterns were analyzed and compared to reference patterns using the Rigaku PDXL software. The peak representing the (1-11) plane of Mo₂C was chosen for Scherrer analysis as there are no overlapping support peaks on any studied material located around 39.4° 2θ .

All thermogravimetric analysis and mass spectrometry (TGA-MS) experiments were performed using a TA Instrument Q500 TGA that was coupled to a Hiden Analytical HPR-20 benchtop mass spectrometer. Approximately 50 mg of sample was added for each analysis. Nitrogen was used as the purge gas, flowing at a rate of 200 mL/min. Each run was comprised of a 30-minute equilibration stage at room temperature before the sample was heated to 750 °C at a rate of 5 °C/min. The products released from the sample during heating were monitored in real-time by mass spectrometry over a m/z range of 2-120. All ions were detected using an ionization energy of 70 eV. The TGA spectra were analyzed using the TA Universal software while the mass spectra were analyzed using the EGAsoft package.

BET surface area analysis was conducted through N₂ adsorption experiments using a Beckman-Coulter S.A. 3100 Surface Area Analyzer. Prior to the experiment, all powders were degassed at 120 °C for 15 minutes under vacuum. All surface area analyses were conducted in liquid N₂ (-196 °C).

CO pulse chemisorption experiments were run using a Micromeritics Autochem II equipped with a thermal conductivity detector. Approximately 150 mg of catalyst were loaded into a quartz U-tube containing a plug of glass of wool. The sample was heated under H₂ to 300 °C for 1.5 hours to mirror the pre-treatment catalytic conditions. After 1.5 hours, the gas flow was changed to helium and the sample was allowed to cool to room temperature. Once at room temperature, the furnace was removed and the quartz tube

was submerged into a dewar containing a dry-ice/iso-propanol bath (~ -70 °C). Once the temperature had stabilized, CO pulse chemisorption experiments were started using He as a reference gas flowing at 50 mL/min. In total, 10 pulses of 10% CO/He were introduced over the sample with 5 minutes programmed in between each pulse where the sample loop had a volume of 0.035 cm³. The total amount of CO absorbed was then used to calculate the amount of active Mo sites assuming that one molecule of CO absorbed to one active Mo site.^{55,56}

Temperature programmed oxidation and temperature programmed desorption experiments were conducted using a Micromeritics Autochem II equipped with a thermal conductivity detector and mass spectra were obtained using a Hiden Analytical HPR-20 benchtop mass spectrometer. Approximately 100 mg of catalyst powder was loaded into a quartz U-tube that was plugged with glass wool. The sample was heated to 300 °C under flowing H₂ for 1 hour to mirror the pre-treatment catalytic conditions. For the TPD experiments, CO₂ was flowed over the catalyst for 1 hour, before He was introduced and the temperature was ramped to 300 °C. For the TPO experiments, a 10% blend of CO₂ in He was introduced and the sample was allowed to equilibrate for minutes before being heated to 350 °C. The collected mass spectra were analyzed using the EGAsoft package.

3.5 Computational Modelling:

Calculations were performed using the Vienna ab initio Simulation Package (VASP).⁵⁷ The Perdew-Burke-Ernzerhof (PBE) generalized gradient approximation was employed as the electron exchange correlation functional using the PBE projector augmented-wave (PAW) potentials.^{58,59} The electronic energy threshold was set at 10⁻⁶ eV while the ionic force threshold was set at 0.02 eV Å⁻¹. While hybrid functionals are widely utilized to model both semiconductors and insulators, the use of these functionals were not employed for this study due to the metallic nature of Mo₂C. All calculations used the Monkhorst-Pack k-points mesh sampling where the bulk slabs utilized a k-point grid of 3 x 3 x 1 while the Mo₂C ribbon supported on MgO utilized a k-point grid of 1 x 3 x 1.⁶⁰

The lattice parameters of the orthorhombic Mo₂C unit cell were 4.743 x 6.058 x 5.231 Å where each unit cell contained 12 atoms arranged in 2 Mo layers (4 Mo in each layer) and 2 C layers (2 atoms in each layer). The bulk slab of Mo₂C(100) was composed of 8 unit cells arranged in a (2 x 2) supercell with dimensions of 9.486 x 12.116 x 10.461 Å and a total of 96 atoms. This slab was optimized and relaxed with a vacuum space of 58.0 Å. Meanwhile, the slab of MgO(111) was terminated on both sides by oxygen to mitigate the inherent polarity of the (111) facet. The (2 x 2) supercell of MgO(111) had dimensions in the a and b directions of 10.318 and 11.914 Å, respectively. In the c direction, the MgO(111) slab was 12 layers thick, or 6 unit cells composed of alternating layers of Mg and O with a vacuum space of 53.2 Å.

A simple model of Mo₂C/MgO was developed by using the optimized MgO(111) and Mo₂C(100) slabs described above with slight adjustments to the Mo₂C slab. These two surfaces were initially chosen because of the good overlap between the lattice parameters which would help mitigate any large atomic rearrangements. Firstly, the (2 x

2) Mo₂C(100) supercell was rotated such that it was aligned with the MgO(111) surface. Additionally, one carbon layer (8 atoms) was removed from one side of the Mo₂C supercell such that the film was terminated by Mo on both sides resulting in a slab with a total of 88 atoms. The slabs were then modelled such that the vacuum distance between the two films was approximately 18 Å. The overall structure was composed of 264 atoms (96 magnesium, 80 oxygen, 24 carbon, and 64 molybdenum) and had unit dimensions of 11.987 x 10.381 x 65 Å. The vacuum gap between the two films was then decreased to 1.8 Å while the vacuum gap on the other side of the structure was increased to 44.5 Å to preserve the z-axis unit dimension of 65 Å. All atoms in the Mo₂C layer were allowed to relax along with top two layers of the MgO surface and the final separation distance between the two slabs after relaxation was approximately 1.5 Å. The ribbon of Mo₂C supported on MgO was then generated by removing half of the Mo₂C slab which resulted in a (1 x 2) Mo₂C supercell on the surface of MgO(111). Molecules of CO₂ and CO were placed at various positions on the surface of both Mo₂C(100) and the oxygen-terminated MgO(111) to determine the optimal adsorption sites for each molecule. Additionally, for the Mo₂C ribbon supported on MgO, molecules of CO₂ and CO were placed parallel to the Mo₂C ribbon and approximately 2 Å above the surface. These structures were allowed to relax and the adsorption energies were calculated by the following: $E_{\text{ads}} = E_{\text{slab+molecule}} - E_{\text{molecule}} - E_{\text{slab}}$.

Table 1 Calcination and carburization temperatures, average Mo₂C particle size, and BET surface areas with and without K-Mo₂C for each support.

	Calcination Temperature (°C)	Carburization Temperature (°C)	Particle Size (nm)	BET Surface area w/out Mo ₂ C (m ² /g)	BET Surface area w/ Mo ₂ C (m ² /g)
Al ₂ O ₃	350	650	7	201.5	116.1
SiO ₂	450	700	12	409.4	195.8
ZrO ₂	600	750	23	32.2	14.9
CeO ₂	650	725	28	31.0	3.6
MgO	450	750	21	29.6	18.8

4.0 Results and Discussion:

4.1 Synthesis and Characterization:

Table 2 Molybdenum oxides identified by XRD post-calcination for each support

Material	Molybdenum Oxides
Al ₂ O ₃	K ₂ MoO ₄ , KAl(MoO ₄) ₂ , MoO ₃
SiO ₂	K ₂ Mo ₄ O ₁₃ , MoO ₃
ZrO ₂	Zr(MoO ₄) ₂ , K ₂ MoO ₄ , MoO ₃
CeO ₂	KCe(MoO ₄) ₂
MgO	K ₁₀ Mg(Mo ₇ O ₂₇)

The selected calcination temperatures for each material were determined through TGA-MS and are reported in Table 1. For instance, mass loss associated with oxidation of the molybdate precursor was observed at temperatures upwards of 610 °C for

CeO₂ but only 400 °C for MgO. As such, the calcination temperatures reported in Table 1 were chosen to be slightly greater than those observed by TGA-MS to ensure the

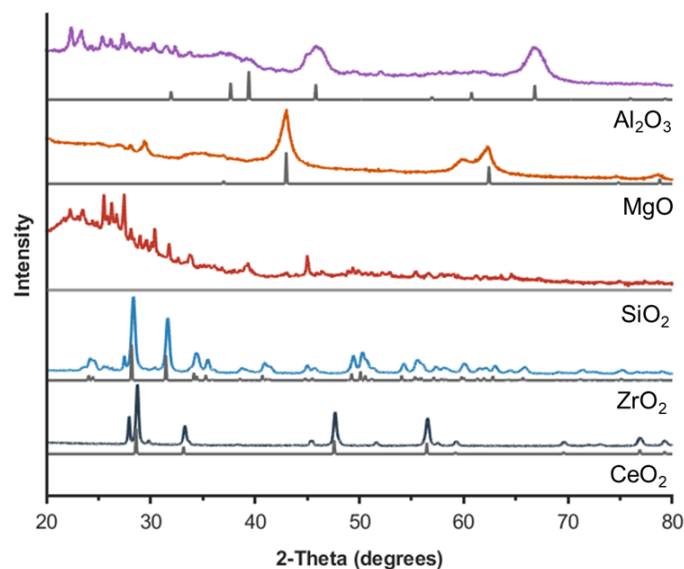


Fig. 1 XRD patterns post-calcination depicting formed molybdenum oxides on the various metal oxide supports. The experimental patterns are shown in color while the corresponding metal oxide reference patterns are shown in gray.

complete oxidation of the molybdate precursors. The range of temperatures reported indicates that the support influences the oxidation of the molybdenum precursor. The XRD patterns of the materials post-calcination but prior to the carburization process are shown in Fig. 1. The formation of a variety of different molybdenum mixed-metal oxides are readily observed and the various phases that were formed are tabulated in Table 2.

After oxidation, the supported catalysts were then carburized at elevated temperatures with a 4:1 blend of $H_2:CH_4$ to transform the molybdenum oxides into Mo_2C . The carburization temperature for each catalyst was

determined by monitoring the effluent stream for CO using online gas chromatography. To determine the carburization temperature required for the respective catalyst/support combinations, the temperature was initially set at 650 °C, then ramped every 45 minutes at intervals of 25 °C until a CO signal was observed, indicating the formation of Mo_2C .^{61,62} The carburization temperatures applied for each catalyst/support combination are also shown in Table 1. Directly following the carburization step, all samples except for the K- Mo_2C/CeO_2 were treated at 600 °C under flowing H_2 to remove any excess carbon that may have deposited.¹⁶ It was found that upon subjection to this H_2 treatment step, the K- Mo_2C/CeO_2 sample was partially reduced from Mo_2C to metallic Mo (Fig. 2). When reducible oxide supports are exposed to reducing environments at elevated temperatures, the metal cations are often reduced which can ultimately promote electron transfer from the support to the deposited metal. The electronic contributions from the strong metal support interaction (SMSI) can thus help to rationalize the observed reduction of Mo_2C to Mo on CeO_2 upon exposure to H_2 at elevated temperatures.^{63–66}

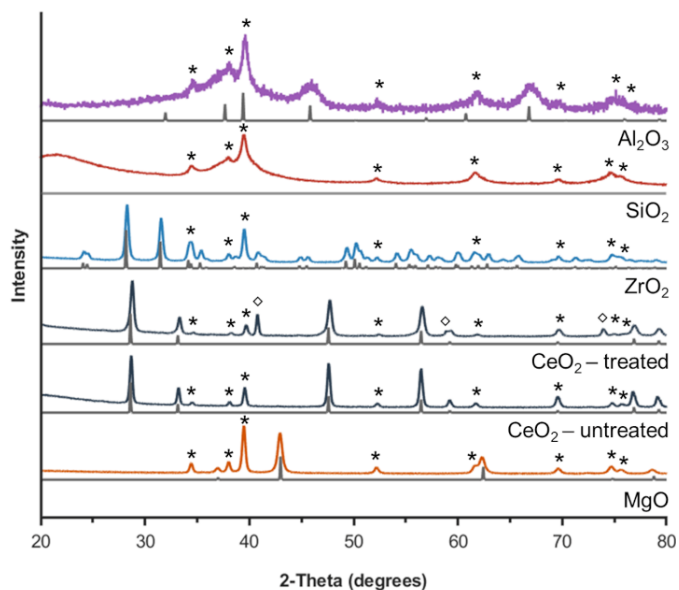


Fig. 2 Experimental XRD patterns showing K- Mo_2C supported on Al_2O_3 , SiO_2 , ZrO_2 , CeO_2 , and MgO . The grey patterns represent the corresponding metal oxide reference patterns while the diamonds and * represent metallic Mo and Mo_2C peaks, respectively.

Experimental XRD patterns (colored) for the supported K-Mo₂C materials along with the corresponding metal oxide reference patterns (gray) are presented in Fig. 2. All samples showed sharp peaks that are indicative of highly crystalline Mo₂C, denoted by asterisks, along with signatures corresponding to the respective metal oxide supports. Due to the amorphous nature of silica, no reference pattern is included for the SiO₂ support. While the asterisks shown in Fig. 2 denote an orthorhombic Mo₂C (β -Mo₂C) reference pattern, the presence of hexagonal Mo₂C (α -Mo₂C) cannot be entirely dismissed due to the challenge of selectively synthesizing one particular phase as well as similarities in the reference XRD reference patterns for α - and β -Mo₂C. Though β -Mo₂C is more extensively studied, both phases have been shown to be catalytically active.^{67,68} The lack of XRD peaks corresponding to any MoO_x or bimetallic oxide species indicated that the selected temperatures for carburization were appropriate to achieve complete conversion to the desired Mo₂C phase for all of the supported catalysts. Additionally, the XRD patterns showed that the reduction of the deposited carbon at 600 °C, with the exception of CeO₂, did not significantly reduce the bulk Mo₂C phase to metallic Mo. Experiments to synthesize K-Mo₂C supported on TiO₂ were also attempted using calcination and carburization temperatures of 350 °C and 750 °C, respectively. However, the experimental XRD pattern (Fig. 3) indicated a mixed-phase population with phases such as Mo₂C and various oxides including titanium molybdates and potassium titanates. The presence of the impurity oxides is most likely attributed to both the mobility of the oxygen vacancies in TiO₂ as well as the increased diffusion rate of the deposited metals at elevated temperatures.^{69–71}

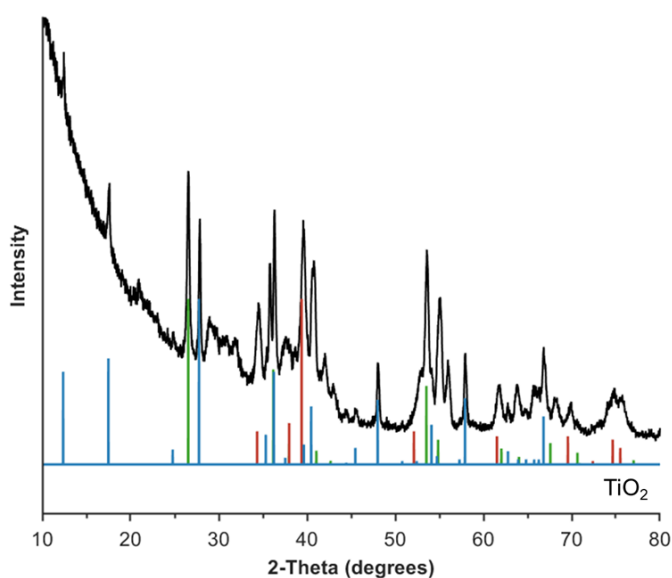


Fig. 3 Experimental XRD pattern of K-Mo₂C/TiO₂ (black) with the associated reference patterns of TiMoO₄ (green), KTi₄O₈ (blue), and Mo₂C (red). The remaining unidentified peaks could not be matched to a reference pattern but are most likely ascribed to other molybdenum or titanium-base metal oxides.

The Mo₂C crystallite sizes were calculated from the experimental XRD patterns using the Scherrer equation and can be seen in Table 1. The smallest calculated Mo₂C size was 7 nm which corresponded to Mo₂C deposited on γ -Al₂O₃. CeO₂ had the largest calculated Mo₂C size of 28 nm. The other supports including SiO₂, MgO, and ZrO₂ showed calculated Mo₂C particle sizes of 12, 21, 22, and 23 nm, respectively. The surface areas for both the unloaded and loaded supports were determined by BET analysis and the results are also presented in Table 1. The measured surface area of the loaded and carburized supports decreased by approximately 50% when compared to bare supports without metal loading. In particular, CeO₂ exhibited a more drastic change, exhibiting nearly a 10-fold drop in the measured surface area which is most likely due to the ripening of the Mo₂C particles. In general, the calculated particle size of Mo₂C was inversely correlated with the measured BET surface area. This result is intuitive as high surface

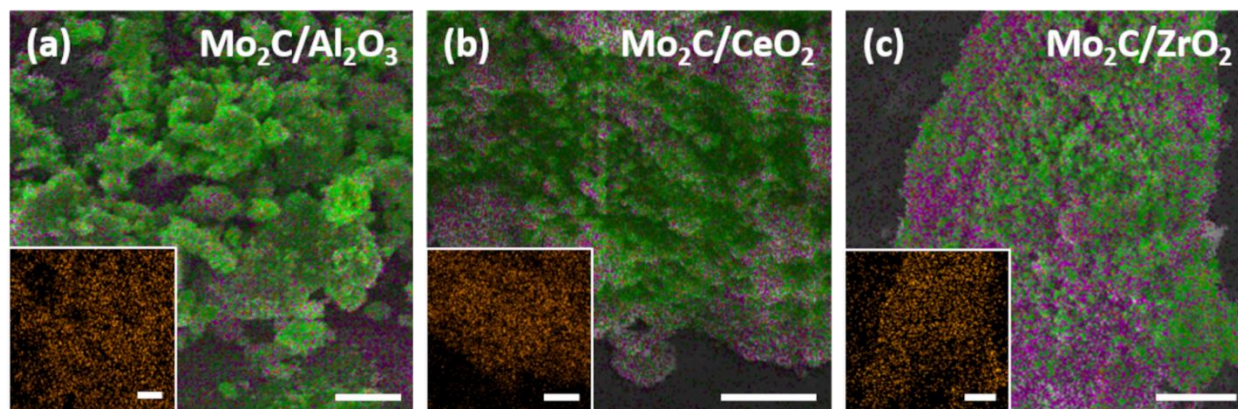


Fig. 4 Overlaid SEM/EDS maps of Mo₂C supported on a) Al₂O₃, b) CeO₂, and c) ZrO₂ where green represents Mo and purple represents the support metal (Al, Ce, or Zr). The potassium elemental maps are shown in orange in the insets for each image. The scale bars represent 2 μm.

area supports tend to produce smaller particles due to the increased amount of surface sites available for nucleation.

To determine the distribution of potassium and molybdenum on the support post-carburization, the materials were further characterized by SEM-EDS. Representative elemental maps for K-Mo₂C on select supports are shown in Fig. 4. The potassium maps (Insets, Fig. 4) demonstrate that potassium was homogeneously distributed with no large aggregates being detected. In contrast, molybdenum tended to aggregate in particular areas on each support. The large difference between the agglomerate sizes observed in the SEM-EDS micrographs and the small particle sizes calculated by the Scherrer equation indicates that the Mo₂C is either polycrystalline or composed of smaller Mo₂C particles which are beneath the resolution limit of the SEM.

4.2 Catalytic Results:

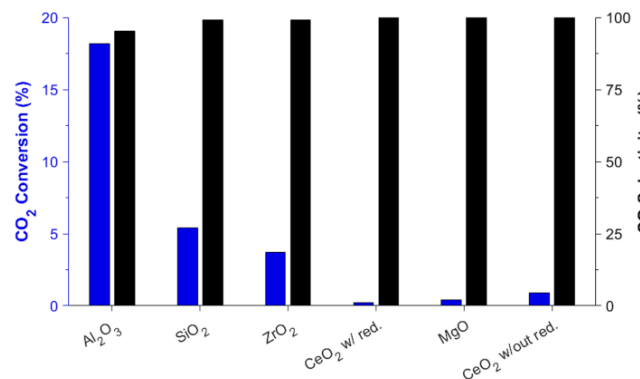


Fig. 5 CO₂ conversion (blue) and CO selectivity (black) of K-promoted Mo₂C supported on various metal oxides at a WHSV of 2 mL s⁻¹ g⁻¹.

For a typical catalytic experiment, the catalyst bed was exposed to a flowing blend of 3:1 H₂:CO₂ at 300 °C, and a pressure of 19.3 bar. The CO₂ conversions and product selectivity for K-promoted Mo₂C deposited on various metal oxide supports are presented in Fig. 5 at a WHSV of 2 mL s⁻¹ g⁻¹. Under these conditions, the K-promoted Mo₂C/Al₂O₃ catalyst demonstrated the highest CO₂ conversion at 18.2% with a selectivity towards CO of 95.2% and the remaining balance composed of CH₄.

This result aligns well with prior reports that also show high CO₂ conversions for Mo₂C and a significant increase in CO selectivity with the use of alkali metal promoters such as potassium. K-promoted Mo₂C supported on ZrO₂ and SiO₂ were also found to be active with CO₂ conversions of 5.4% and 3.7%,

Table 3 Mo active sites ($\mu\text{mol/g}$) determined by CO pulse chemisorption and the CO STY (min^{-1}).

	Mo active sites ($\mu\text{mol/g}$)	CO STY (min^{-1})
Al_2O_3	5.6	55.6
SiO_2	2.9	23.3
ZrO_2	2.0	18.6
MgO	0.7	2.7
CeO_2 – w/out reduction	0.8	0.9

respectively with 99.1% and 99.2% CO selectivity, respectively. K-Mo₂C/CeO₂ that was not treated with H₂ directly following carburization showed slightly lower conversions than K-Mo₂C/CeO₂ that was treated with H₂ though both conversions, along with MgO, were <1%, albeit with no observed methane production. The reduced conversion over the untreated K-Mo₂C/CeO₂ is attributed carbon leftover from the carburization process that is blocking active sites while the low conversions over the treated K-Mo₂C/CeO₂ is attributed to the presence of Mo metal which is inactive for the RWGS.⁷²

In order to compare the intrinsic activity of Mo₂C on different supports, CO pulse chemisorption was used to determine the number of Mo active sites per gram of material which was then used to calculate the CO site time yield (STY). The results of the CO pulse chemisorption experiments can be seen in Table 3. K-Mo₂C supported on CeO₂ that was subjected to the H₂ treatment was calculated to have the greatest density of Mo active sites at 5.6 $\mu\text{mol/g}$. However, this is likely an overestimate compared to the true quantity of catalytically active sites as metallic Mo, which is inactive for the RWGS reaction, is also known to adsorb CO under these conditions.⁵⁶ For that reason, this sample was omitted from Table 3. Comparatively, the K-Mo₂C/CeO₂ that was not exposed to the H₂ treatment and thus exhibited no detectable metallic Mo by XRD, was calculated to have a Mo active site density of 0.8 $\mu\text{mol/g}$. Meanwhile, active site densities for K-Mo₂C supported on γ -Al₂O₃ and SiO₂ were 5.6 and 2.9 $\mu\text{mol/g}$, respectively. Furthermore, K-Mo₂C supported on ZrO₂ and MgO had active site densities of 2.0 and 0.7 $\mu\text{mol/g}$, respectively.

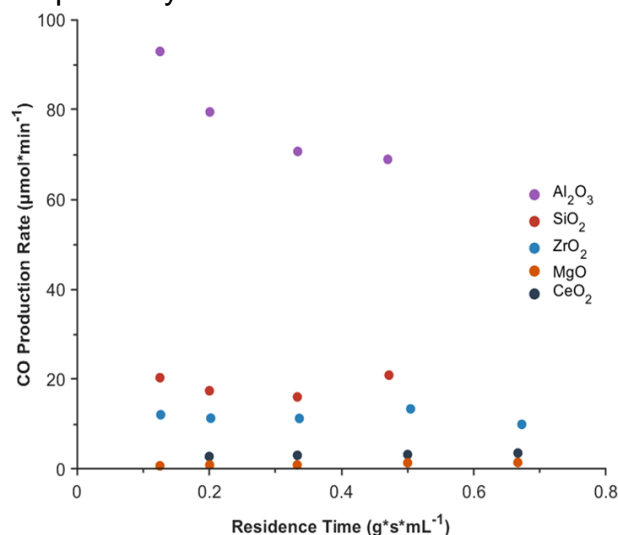


Fig. 6 The production rate of CO as a function of residence time for K-Mo₂C supported on various metal oxide supports. The CO turnover frequency was extracted from the y-intercept of the best fit line that was generated from data points at the three lowest residence times for each catalyst/support system.

Utilizing the Mo active site data, the CO STY for each material was determined by conducting a sweep of different space velocities (Fig. 6). To ensure that the supported catalysts were not limited by diffusion, the CO production rate at the three lowest residence times were chosen to generate a line of best fit, from which the y-intercept was used, along with the amount of Mo active sites and the total mass of catalyst, to calculate the CO STY values shown in Table 3. The STY values followed a similar trend to the CO₂ conversion rate with K-Mo₂C/Al₂O₃ exhibiting the highest CO STY of 55.6 min^{-1} . Both K-Mo₂C/SiO₂ and K-Mo₂C/ZrO₂ had similar values of 23.3 and 18.6 min^{-1} , respectively. MgO and CeO₂, which were found to have the lowest

CO₂ conversions, were also found to have the lowest CO STY values. It is important to note that the STY values reported for K-Mo₂C/CeO₂ are for the sample that was not subjected to the hH₂ treatment. The STY values for the H₂ treated samples are not included as a realistic active site density could not be calculated by methods utilized herein for reasons discussed previously. As discussed in more detail below, the CO STY values shown in Table 3 indicate that the rate of CO production is dependent on the identity of the metal oxide support with non-reducible and more acidic oxides displaying higher STY values than reducible and basic oxides.

It has been previously demonstrated that the RWGS activity over metals such as Pt and Cu is greatly increased when supported on reducible oxides like CeO₂ and TiO₂.^{26,71,73} However, our results appear to contrast with these trends as K-Mo₂C supported on the non-reducible oxides studied in this work are significantly more active than K-Mo₂C supported on reducible oxides. This outcome could be attributed to the different preparation methods employed for supported zero-valent metals compared to supported transition metal carbides. For instance, supported zero-valent metals are often calcined in air prior to testing.^{71,73} This ensures that both the metal oxide support is fully oxidized and that any SMSI induced overlayer encapsulating the catalyst particles is also removed. However, in the case of supported transition metal carbides, this calcination step is infeasible as the desired carbide phase would readily transform into the corresponding oxide. Under the utilized preparation conditions for supported TMCs that involve high temperatures and reducing environments, reducible oxide supports are expected to have an increased number of oxygen vacancies and exhibit reduction of the cationic metal of the oxide.^{46,66,74} This is believed to allow for electron transfer between the support and the deposited catalyst due to the SMSI.^{66,74,75} This can help to rationalize the “over-reduction” of Mo₂C to metallic Mo on CeO₂. However, this phenomenon would be less impactful for the aforementioned supported zero-valent metals as the active phase is the fully reduced species. On the contrary, when Mo₂C is supported on non-reducible oxides such as Al₂O₃ or SiO₂, the carbide phase is stable and active for the RWGS.

As suggested by prior literature, our results also indicate that the acidity of the metal oxide support also appears to affect the measured catalytic activity.^{50,53} Both γ -Al₂O₃ and ZrO₂ are generally considered to have prominent Lewis acid character. Furthermore, SiO₂ is classified as weakly acidic, MgO as basic, and CeO₂ has both weakly acidic and strongly basic properties.^{76–78} The acidity of the support trends well with the CO STYs reported in Table 3 meaning that more acidic supports such as γ -Al₂O₃, SiO₂, and ZrO₂ have higher CO STYs than supports that are basic such as MgO. These acidic supports are thought to stabilize reaction intermediates including formates or carboxylates.^{46,79} Conversely, MgO contains strong Lewis basic sites which heavily favors the adsorption of CO₂.^{80,81} It is hypothesized that the strong interaction between the acidic CO₂ molecule and the basic MgO surface leads toward a Lewis acid-base adduct that inhibits the RWGS activity for Mo₂C catalysts and results in the low CO STYs observed. Finally, while CeO₂ is an amphoteric support and it is anticipated that the exposed acid sites do promote RWGS activity, the poor activity observed is likely attributed to the SMSI effects rather than the amphoteric nature of the CeO₂ support.

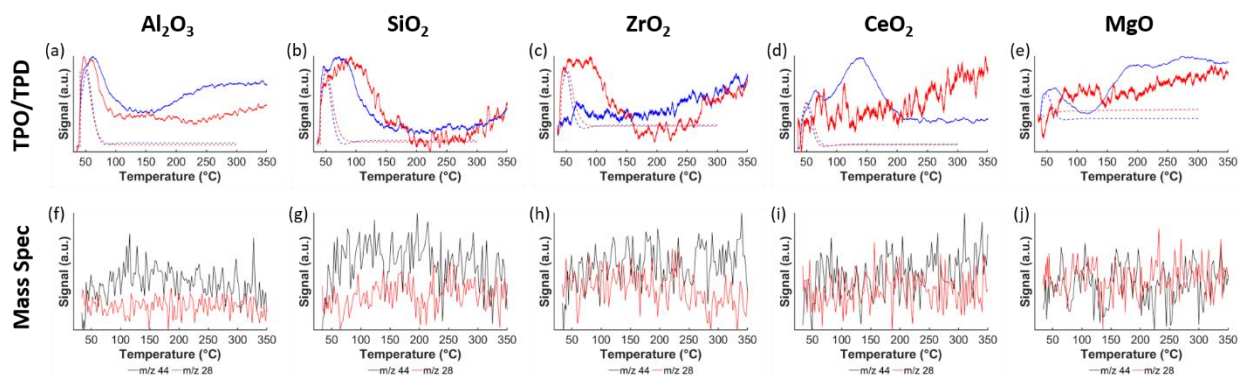


Fig. 7 Temperature programmed oxidation (solid lines) and temperature programmed desorption (dashed lines) experiments for the bare metal oxide supports (blue) and supported K-Mo₂C materials (red) are shown in the top row. The corresponding mass spectra for m/z 44 and 28 are shown in the bottom row for supported K-Mo₂C. No significant increase in m/z 28 signal was observed indicating that either Mo₂O_xC_y was not formed or the subsequent formation of CO was below the detectable limits of the mass spectrometer.

Prior studies have reported that molybdenum oxycarbide (Mo₂C-O) formed under operating conditions enhances the observed RWGS activity.^{30,34,82,83} The formation of the Mo₂C-O is thought to arise from the interaction of CO₂ with Mo₂C which forms CO and the oxycarbide phase. The Mo₂C-O can then be reduced by H₂ to regenerate the Mo₂C surface with the concomitant formation of water.³⁰ To probe whether the evolution of Mo₂C to the oxycarbide species is not support dependent and that the observed TOF differences was due to the support acidity and reducibility, temperature programmed oxidation experiments coupled with mass spectrometry (Fig. 7 a-e). Overall, no significant changes were observed in either the m/z = 44 or m/z = 28 (Fig. 7 f-i) signals which indicated that molybdenum oxycarbide had either not formed or was below the instrumental limit of detection. This corresponds well with prior reports that have indicated that only the first few surface layers of Mo₂C may undergo transformation to the oxycarbide as the bulk structure is thermodynamically unstable.⁸⁴ Further in-situ characterization methods would therefore be highly beneficial to fully understand any role the metal oxide support may have on the formation of a surface molybdenum oxycarbide phase.

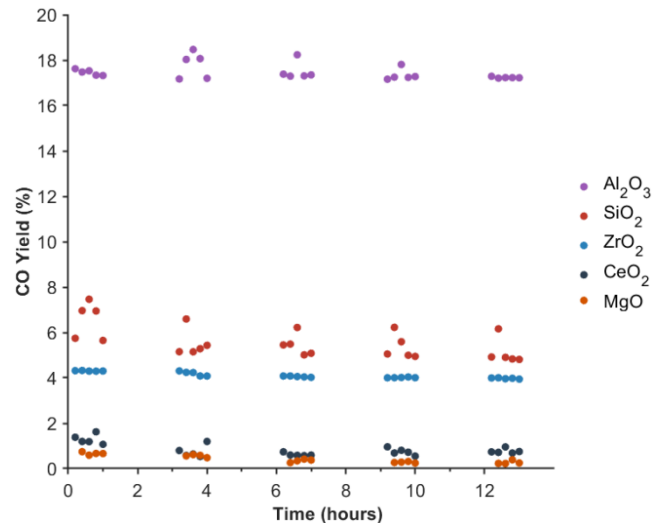


Fig. 8 Time on stream studies for K-promoted Mo₂C supported on various metal oxides at 300 °C and a WHSV of 2 mL s⁻¹ g⁻¹.

To determine the stability of the supported Mo₂C catalysts under operating conditions, time on stream studies were conducted over the course of 13 hours for each catalyst at a WHSV of 2 mL s⁻¹ g⁻¹ and the results are presented in Fig. 8. While small decreases in the CO yield were initially observed for each material, the performance of each catalyst/support over 13 hours had minimal variations indicating that all 5 materials were stable. This corresponds well with prior reports from Juneau et al. and Sun et al. that demonstrated K-promoted Mo₂C/Al₂O₃

was stable under RWGS operating conditions for at least 10 days or 100 hours, respectively.^{22,85}

4.3 DFT Modelling:

Table 4 Calculated CO₂ and CO adsorption energies from computational models of Mo₂C(100), MgO(111), and Mo₂C/MgO. The * denotes two different CO adsorption configurations for Mo₂C/MgO(111).

	CO ₂ Adsorption Energy (eV)	CO Adsorption Energy (eV)
Mo ₂ C(100)	-1.6	-2.7
MgO(111)	-0.09	-5.6
Mo ₂ C/MgO – a*	-0.9	-0.7
Mo ₂ C/MgO – b*	N.A.	-4.3

DFT modelling was conducted to further probe supports effects on the adsorption energies of CO₂ and CO on Mo ribbons. In particular, MgO was selected as the model support due to its rocksalt structure and lattice parameter

overlap with Mo₂C(100). After relaxing the Mo₂C(100) and MgO(111) slabs, CO₂ and CO were placed above both surfaces and allowed to relax with the resulting adsorption energies being tabulated in Table 4. For the Mo₂C(100) slab, both CO₂ and CO adsorb to surface with energies of -1.63 and -2.66 eV, respectively (Fig. 9a and b). When CO₂ is placed above the bare MgO(111) surface (Fig. 9c), there is minimal interaction as indicated by an adsorption energy of -0.09 eV. Upon placing CO above the MgO(111) surface, it was observed that the CO molecule strips an oxygen from the MgO surface to form CO₂ (Fig. 9d) indicating that the formation of CO₂ was more favorable compared to the adsorption of CO. The calculated energy of this system was -5.6 eV though this was mainly attributed to the formation of the CO₂ molecule.

The Mo₂C(100) and MgO(111) surfaces were then combined such that a ribbon of Mo₂C(100) was attached to the surface of the MgO(111) slab. The optimal separation distance between the two slabs that resulted in the lowest “bulk” energy was determined to be approximately 1.5 Å. This separation distance was observed even when the Mo₂C and MgO slabs were initially separated by a distance of 4 Å. To ensure that the Mo₂C ribbon and MgO slabs were electronically interacting at the selected separation distance of 1.8 Å, a charge density distribution (CDD) map was generated using VESTA and can be seen in Fig. 10.⁸⁶ The yellow surfaces represent areas of increased electron density while the blue surfaces represent areas of decreased electron energy. The CDD map demonstrates that there are significant electronic perturbations at the MgO/Mo₂C interface, indicating that the two slabs are not electronically isolated but are indeed interacting. Molecules of

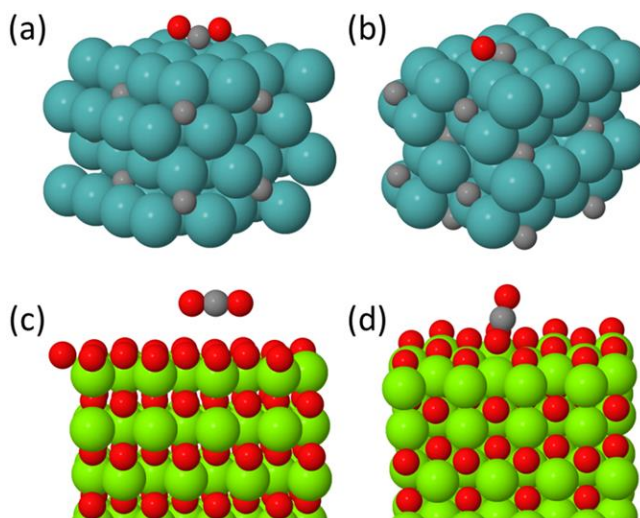


Fig. 9 Computational models showing the interaction of CO₂ and CO when placed on bulk slabs of (a,b) Mo₂C(100) and (c,d) MgO(111). The green spheres represent Mg, the red spheres represent O, the blue spheres represent Mo, and the gray spheres represent carbon.

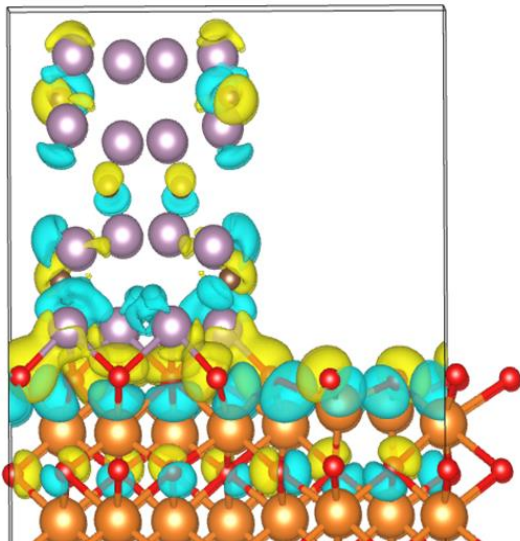


Fig. 10 Charge density difference of the Mo₂C(100) ribbon on top of the O-terminated MgO(111) slab. The yellow isosurfaces are indicative of areas with increased electron density whereas the blue isosurfaces indicate areas with decreased electron density.

CO₂ and CO were then placed near the Mo₂C and MgO interface with the resulting adsorption energies being tabulated in Table 4. For CO₂, the adsorption energy was found to be -0.90 eV with an oxygen from CO₂ interacting with two Mo atoms in the Mo₂C ribbon and the carbon interacting with three oxygens, one of which is from the MgO surface layer (Fig. 11a). Interestingly, when CO was placed at the interface of Mo₂C/MgO and allowed to relax, two unique structures were observed. The first structure shows a bidentate adsorption to two surface O atoms with the O from the CO being stabilized by the Mo in the Mo₂C ribbon with an adsorption energy of -4.34 eV (Fig. 11b). The second structure shows a monodentate adsorption of CO to the MgO surface with a less favorable adsorption energy of -0.66 eV (Fig. 11c).

From these results, it was concluded the adsorption energies of CO₂ and CO are markedly different when adsorbed at the Mo₂C/MgO interface when compared to the bulk MgO(111) or Mo₂C(100) surfaces. For instance, the binding of CO₂ and CO to the pure Mo₂C(100) slab showed favorable adsorption while on the MgO(111) surface, the adsorption was unfavorable for both adsorbates with the adsorbed CO molecule interacting with a lattice oxygen to form CO₂. However, when CO₂ and CO were placed at the Mo₂C/MgO interface, the adsorbates were found to interact with both surfaces. In particular, both adsorbates showed structures that contained a carbonate-like motif that interacted with the Mo₂C ribbon as well as the MgO support. The main difference between the two structures was that adsorbed CO interacted with two oxygens at the MgO surface while CO₂ only interacted with one surface MgO oxygen. This resulted in C-O bond distances that were on average shorter for the carbonate motif formed from CO than CO₂.

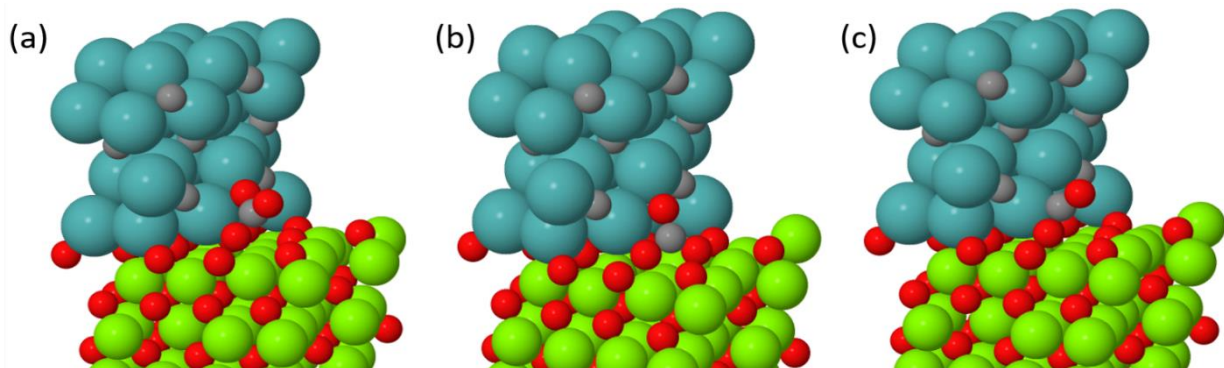


Fig. 11 Computation models depicting the adsorption of a) CO₂ and b,c) CO at the Mo₂C(100)/MgO(111) interface with green spheres representing Mg, red spheres representing O, blue spheres representing Mo, and gray spheres representing carbon.

Additionally, the shorter C-O bond distances also correlated well with significantly increased adsorption energies for CO ('Mo₂C/MgO – a' in Table 4) compared to CO₂. The large adsorption energies observed for CO at the interface in this arrangement could help to explain the poor experimental activity discussed in section 4.2 with the hypothesis that CO is strongly bound to the surface, which would inhibit catalytic activity. Therefore, the assumption that CO only adsorbs to the Mo sites in a 1:1 ratio may not be accurate for the Mo₂C/MgO system. Finally, CO was shown to have another unique structure when adsorbed at the Mo₂C/MgO interface which involved a monodentate binding of CO to the MgO surface. Unlike when CO was placed on the bulk MgO(111) surface, the calculated structure did not result with a MgO lattice oxygen being displaced from the surface to form CO₂. This implies that the nearby Mo₂C ribbon helps to stabilize the CO on the MgO surface, potentially through Mo-C interactions.

Further modelling is needed to systematically study how other low index facets of MgO such as the (110) and (100) interact with ribbons of Mo₂C on the surface as well as the influence these facets may have on the adsorption of CO₂ and CO. Furthermore, expansion to other oxide support systems could help to elucidate the role of the support in influencing the RWGS activity observed for Mo₂C.

5.0 Conclusions:

Potassium promoted molybdenum carbide was supported on various metal oxides to determine the role that support acidity and reducibility have on the RWGS activity. To accurately compare the materials against each other, the CO STY normalized for the Mo active site density was determined for each catalyst/support system. Our results indicated that CO STYs are greater for K-Mo₂C when supported on acidic, non-reducible metal oxides while reducible oxide supports do not lead to greater CO STY's for K-Mo₂C. For instance, supports that contained acidic sites such as γ -Al₂O₃ or ZrO₂ were considerably more active than those containing numerous basic sites like MgO. Meanwhile, when K-Mo₂C was supported on a reducible support such as CeO₂, the Mo₂C was over-reduced to metallic Mo which significantly hindered the observed RWGS activity. Accordingly, the non-reducible and Lewis acidic support γ -Al₂O₃, was determined to be the best performing metal oxide support of those studied herein, for the K-Mo₂C catalyst with a CO STY of 55.6 min⁻¹. Finally, computational modelling for Mo₂C supported on MgO provided insights into the low activity observed over the catalyst. When CO is adsorbed at the interface, the formation of a carbonate-like motif was observed, leading to the hypothesis that CO may be poisoning active sites of the K-Mo₂C/MgO catalyst which further explains the poor activity. Additional investigations are currently underway that utilize DFT modelling to further understand support effects and their influence on the K-Mo₂C RWGS activity.

6.0 References:

- 1 J. A. Turner, *Science*, 1999, **285**, 687–689.
- 2 N. S. Lewis and D. G. Nocera, *Proc. Natl. Acad. Sci.*, 2006, **103**, 15729–15735.

- 3 B. Yu and L.-N. He, *ChemSusChem*, 2015, **8**, 52–62.
- 4 J. Keasling, H. Garcia Martin, T. S. Lee, A. Mukhopadhyay, S. W. Singer and E. Sundstrom, *Nat. Rev. Microbiol.*, 2021, **19**, 701–715.
- 5 P. Mehta, P. Barboun, F. A. Herrera, J. Kim, P. Rumbach, D. B. Go, J. C. Hicks and W. F. Schneider, *Nat. Catal.*, 2018, **1**, 269–275.
- 6 W.-H. Wang, Y. Himeda, J. T. Muckerman, G. F. Manbeck and E. Fujita, *Chem. Rev.*, 2015, **115**, 12936–12973.
- 7 M. D. Porosoff, B. Yan and J. G. Chen, *Energy Environ. Sci.*, 2016, **9**, 62–73.
- 8 S. Nitopi, E. Bertheussen, S. B. Scott, X. Liu, A. K. Engstfeld, S. Horch, B. Seger, I. E. L. Stephens, K. Chan, C. Hahn, J. K. Nørskov, T. F. Jaramillo and I. Chorkendorff, *Chem. Rev.*, 2019, **119**, 7610–7672.
- 9 Federal Register, EO 14057, 2021, **86**, pp. 70935–70943
- 10 U.S. Department of Defense, Department of Defense Climate Adaptation, Plan, 2021, 1–32.
- 11 H. D. Willauer, F. DiMascio, D. R. Hardy and F. W. Williams, *Energy and Fuels*, 2017, **31**, 1723–1730.
- 12 H. D. Willauer, F. DiMascio, D. R. Hardy, M. K. Lewis and F. W. Williams, *Ind. Eng. Chem. Res.*, 2011, **50**, 9876–9882.
- 13 H. D. Willauer, F. DiMascio, D. R. Hardy, M. K. Lewis and F. W. Williams, *Ind. Eng. Chem. Res.*, 2012, **51**, 11254–11260.
- 14 H. D. Willauer, F. DiMascio, D. R. Hardy and F. W. Williams, *Ind. Eng. Chem. Res.*, 2014, **53**, 12192–12200.
- 15 H. D. Willauer, D. R. Hardy, M. K. Lewis, E. C. Ndubizu and F. W. Williams, *Energy & Fuels*, 2010, **24**, 6682–6688.
- 16 M. D. Porosoff, J. W. Baldwin, X. Peng, G. Mpourmpakis and H. D. Willauer, *ChemSusChem*, 2017, **10**, 2408–2415.
- 17 J. R. Morse, M. Juneau, J. W. Baldwin, M. D. Porosoff and H. D. Willauer, *J. CO2*

- Util.*, 2020, **35**, 38–46.
- 18 M. V. Twigg, *Catalyst Handbook*, 2nd edn., 1989.
 - 19 H.-X. Liu, S.-Q. Li, W.-W. Wang, W.-Z. Yu, W.-J. Zhang, C. Ma and C.-J. Jia, *Nat. Commun.*, 2022, **13**, 867.
 - 20 X. Zhang, X. Zhu, L. Lin, S. Yao, M. Zhang, X. Liu, X. Wang, Y.-W. Li, C. Shi and D. Ma, *ACS Catal.*, 2017, **7**, 912–918.
 - 21 C.-S. Chen, W.-H. Cheng and S.-S. Lin, *Appl. Catal. A Gen.*, 2004, **257**, 97–106.
 - 22 M. Juneau, M. Vonglis, J. Hartvigsen, L. Frost, D. Bayerl, M. Dixit, G. Mpourmpakis, J. R. Morse, J. W. Baldwin, H. D. Willauer and M. D. Porosoff, *Energy Environ. Sci.*, 2020, **13**, 2524–2539.
 - 23 X. Chen, X. Su, H.-Y. Su, X. Liu, S. Miao, Y. Zhao, K. Sun, Y. Huang and T. Zhang, *ACS Catal.*, 2017, **7**, 4613–4620.
 - 24 R. M. Bown, M. Joyce, Q. Zhang, T. R. Reina and M. S. Duyar, *Energy Technol.*, 2021, **9**, 2100554.
 - 25 T. Wang, M. D. Porosoff and J. G. Chen, *Catal. Today*, 2014, **233**, 61–69.
 - 26 S. Kattel, B. Yan, J. G. Chen and P. Liu, *J. Catal.*, 2016, **343**, 115–126.
 - 27 J. Ye, Q. Ge and C. Liu, *Chem. Eng. Sci.*, 2015, **135**, 193–201.
 - 28 J. H. Kwak, L. Kovarik and J. Szanyi, *ACS Catal.*, 2013, **3**, 2094–2100.
 - 29 R. B. Levy and M. Boudart, *Science*, 1973, **181**, 547–549.
 - 30 M. D. Porosoff, X. Yang, J. A. Boscoboinik and J. G. Chen, *Angew. Chemie Int. Ed.*, 2014, **53**, 6705–6709.
 - 31 P. Liu and J. A. Rodriguez, *J. Phys. Chem. B*, 2006, **110**, 19418–19425.
 - 32 H. Zhou, Z. Chen, E. Kountoupi, A. Tsoukalou, P. M. Abdala, P. Florian, A. Fedorov and C. R. Müller, *Nat. Commun.*, 2021, **12**, 5510.

- 33 S. Posada-Pérez, F. Viñes, P. J. Ramirez, A. B. Vidal, J. A. Rodriguez and F. Illas, *Phys. Chem. Chem. Phys.*, 2014, **16**, 14912–14921.
- 34 A. Kurlov, E. B. Deeva, P. M. Abdala, D. Lebedev, A. Tsoukalou, A. Comas-Vives, A. Fedorov and C. R. Müller, *Nat. Commun.*, 2020, **11**, 4920.
- 35 C. G. Silva, F. B. Passos and V. T. da Silva, *J. Catal.*, 2019, **375**, 507–518.
- 36 S. B. Derouane-Abd Hamid, J. R. Anderson, I. Schmidt, C. Bouchy, C. J. H. Jacobsen and E. G. Derouane, *Catal. Today*, 2000, **63**, 461–469.
- 37 F. Solymosi, J. Cserényi, A. Szöke, T. Bánsági and A. Oszkó, *J. Catal.*, 1997, **165**, 150–161.
- 38 H. Vrubel and X. Hu, *Angew. Chemie Int. Ed.*, 2012, **51**, 12703–12706.
- 39 C. Wan, Y. N. Regmi and B. M. Leonard, *Angew. Chemie Int. Ed.*, 2014, **53**, 6407–6410.
- 40 C. Panaritis, M. Edake, M. Couillard, R. Einakchi and E. A. Baranova, *J. CO2 Util.*, 2018, **26**, 350–358.
- 41 D. L. Jurković, A. Pohar, V. D. B. C. Dasireddy and B. Likozar, *Chem. Eng. Technol.*, 2017, **40**, 973–980.
- 42 I. Chorkendorff and J. W. Niemantsverdriet, *Concepts of Modern Catalysis and Kinetics*, Wiley-VCH Verlag, 2003.
- 43 M. Zhu, Q. Ge and X. Zhu, *Trans. Tianjin Univ.*, 2020, 26, 172–187.
- 44 S. J. Tauster, S. C. Fung and R. L. Garten, *J. Am. Chem. Soc.*, 1978, **100**, 170–175.
- 45 A. Goguet, F. C. Meunier, D. Tibiletti, J. P. Breen and R. Burch, *J. Phys. Chem. B*, 2004, **108**, 20240–20246.
- 46 L. F. Bobadilla, J. L. Santos, S. Ivanova, J. A. Odriozola and A. Urakawa, *ACS Catal.*, 2018, **8**, 7455–7467.
- 47 C.-S. Chen, W.-H. Cheng and S.-S. Lin, *Catal. Letters*, 2000, **68**, 45–48.

- 48 M. J. L. Ginés, A. J. Marchi and C. R. Apesteguía, *Appl. Catal. A Gen.*, 1997, **154**, 155–171.
- 49 M. Miyamoto, A. Hamajima, Y. Oumi and S. Uemiya, *Int. J. Hydrogen Energy*, 2018, **43**, 730–738.
- 50 F. Saad, J. D. Comparot, R. Brahmi, M. Bensitel and L. Pirault-Roy, *Appl. Catal. A Gen.*, 2017, **544**, 1–9.
- 51 C. Leyva, M. S. Rana, F. Trejo and J. Ancheyta, *Ind. Eng. Chem. Res.*, 2007, **46**, 7448–7466.
- 52 J. Zhao, H. Chen, J. Xu and J. Shen, *J. Phys. Chem. C*, 2013, **117**, 10573–10580.
- 53 M. Juneau, C. Pope, R. Liu and M. D. Porosoff, *Appl. Catal. A Gen.*, 2021, **620**, 118034.
- 54 H. Sakurai, S. Tsubota and M. Haruta, *Appl. Catal. A Gen.*, 1993, **102**, 125–136.
- 55 J. S. Lee, S. T. Oyama and M. Boudart, *J. Catal.*, 1987, **106**, 125–133.
- 56 J. S. Lee, K. H. Lee and J. Y. Lee, *J. Phys. Chem.*, 1992, **96**, 362–366.
- 57 G. Kresse and J. Furthmüller, *Phys. Rev. B - Condens. Matter Mater. Phys.*, 1996, **54**, 11169–11186.
- 58 J. P. Perdew, K. Burke and M. Ernzerhof, *Phys. Rev. Lett.*, 1996, **77**, 3865–3868.
- 59 P. E. Blöchl, *Phys. Rev. B*, 1994, **50**, 17953–17979.
- 60 H. J. Monkhorst and J. D. Pack, *Phys. Rev. B*, 1976, **13**, 5188–5192.
- 61 T. Xiao, A. P. E. York, V. C. Williams, H. Al-Megren, A. Hanif, X. Zhou and M. L. H. Green, *Chem. Mater.*, 2000, **12**, 3896–3905.
- 62 S. Li, W. B. Kim and J. S. Lee, *Chem. Mater.*, 1998, **10**, 1853–1862.
- 63 C. G. Vayenas, S. Brosda and C. Pliangos, *J. Catal.*, 2003, **216**, 487–504.

- 64 J. Disdier, J.-M. Herrmann and P. Pichat, *J. Chem. Soc. Faraday Trans. 1 Phys. Chem. Condens. Phases*, 1983, **79**, 651–660.
- 65 Q. Fu, T. Wagner, S. Olliges and H.-D. Carstanjen, *J. Phys. Chem. B*, 2005, **109**, 944–951.
- 66 S. J. Tauster, S. C. Fung, R. T. K. Baker and J. A. Horsley, *Science*, 1981, **211**, 1121–1125.
- 67 X. Liu, C. Kunkel, P. Ramírez de la Piscina, N. Homs, F. Viñes and F. Illas, *ACS Catal.*, 2017, **7**, 4323–4335.
- 68 J. W. Han, L. Li and D. S. Sholl, *J. Phys. Chem. C*, 2011, **115**, 6870–6876.
- 69 I. Szenti, L. Bugyi and Z. Kónya, *Surf. Sci.*, 2015, **641**, 60–67.
- 70 B. Domenichini, G. Andrea Rizzi, P. Krüger, M. Della Negra, Z. Li, M. Petukhov, G. Granozzi, P. Juul Møller and S. Bourgeois, *Phys. Rev. B*, 2006, **73**, 245433.
- 71 S. S. Kim, K. H. Park and S. C. Hong, *Fuel Process. Technol.*, 2013, **108**, 47–54.
- 72 A. G. Kharaji, A. Shariati and M. A. Takassi, *Chinese J. Chem. Eng.*, 2013, **21**, 1007–1014.
- 73 S.-C. Yang, S. H. Pang, T. P. Sulmonetti, W.-N. Su, J.-F. Lee, B.-J. Hwang and C. W. Jones, *ACS Catal.*, 2018, **8**, 12056–12066.
- 74 E. W. Zhao, H. Zheng, K. Ludden, Y. Xin, H. E. Hagelin-Weaver and C. R. Bowers, *ACS Catal.*, 2016, **6**, 974–978.
- 75 A. Ruiz Puigdollers, P. Schlexer, S. Tosoni and G. Pacchioni, *ACS Catal.*, 2017, **7**, 6493–6513.
- 76 M. Kumar, F. Aberuagba, J. K. Gupta, K. S. Rawat, L. D. Sharma and G. Murali Dhar, *J. Mol. Catal. A Chem.*, 2004, **213**, 217–223.
- 77 M. K. Gnanamani, R. Garcia, G. Jacobs, K. Góra-Marek, D. C. Cronauer, A. J. Kropf and C. L. Marshall, *Appl. Catal. A Gen.*, 2020, **602**, 117722.
- 78 J. J. Corral-Pérez, C. Copéret and A. Urakawa, *J. Catal.*, 2019, **380**, 153–160.

- 79 A. A. Upadhye, I. Ro, X. Zeng, H. J. Kim, I. Tejedor, M. A. Anderson, J. A. Dumesic and G. W. Huber, *Catal. Sci. Technol.*, 2015, **5**, 2590–2601.
- 80 P. Hu, S. Wang and Y. Zhuo, *Sep. Purif. Technol.*, 2022, **284**, 120253.
- 81 A. O. Menezes, P. S. Silva, E. Padrón Hernández, L. E. P. Borges and M. A. Fraga, *Langmuir*, 2010, **26**, 3382–3387.
- 82 A. Kurlov, X. Huang, E. B. Deeva, P. M. Abdala, A. Fedorov and C. R. Müller, *Nanoscale*, 2020, **12**, 13086–13094.
- 83 A. Kurlov, D. Stoian, A. Baghizadeh, E. Kountoupi, E. B. Deeva, M. Willinger, P. M. Abdala, A. Fedorov and C. R. Müller, *Catal. Sci. Technol.*, 2022, **12**, 5620–5628.
- 84 S. R. J. Likith, C. A. Farberow, S. Manna, A. Abdulslam, V. Stevanović, D. A. Ruddy, J. A. Schaidle, D. J. Robichaud and C. V Ciobanu, *J. Phys. Chem. C*, 2018, **122**, 1223–1233.
- 85 G. Sun, S. Mottaghi-Tabar, L. Ricardez-Sandoval and D. S. A. Simakov, *Top. Catal.*, 2021, **64**, 414–430.
- 86 K. Momma and F. Izumi, *J. Appl. Crystallogr.*, 2011, **44**, 1272–1276.